Polymer 49 (2008) 2924–2936

Contents lists available at ScienceDirect

Polymer

journal homepage: www.elsevier.com/locate/polymer

Theory and kinematic measurements of the mechanics of stable electrospun polymer jets

Matthew E. Helgeson [a], Kristie N. Grammatikos [a], Joseph M. Deitzel [b], Norman J. Wagner [a,*]

[a] Center for Molecular and Engineering Thermodynamics, Department of Chemical Engineering, University of Delaware, 150 Academy Street, Newark, DE 19716, United States
[b] Center for Composite Materials, University of Delaware, Newark, DE 19716, United States

ARTICLE INFO

Article history:
Received 28 December 2007
Received in revised form 14 April 2008
Accepted 15 April 2008
Available online 18 April 2008

Keywords:
Electrospinning
Nanofibers
Rheology

ABSTRACT

We present a simplified approach to understanding the mechanics of stable electrospinning jets based on electrohydrodynamic theory that explicitly incorporates the extensional rheology of polymeric fluids. Flow regimes of electrospun jets are identified by analogy to uniaxial extension of a fluid jet. These flow regimes predict the limiting kinematics of electrospinning jets and identify dimensionless parameters important to the control and operation of electrospinning processes. In situ kinematic measurements validate model assumptions and scaling predictions, and allow the reduction of entire jet radius and velocity profiles to several key parameters. The model predictions are shown to hold both above and below the entanglement concentration, as well as for solutions with added electrolyte and increased conductivity. The analysis also enables direct measurement of the apparent extensional viscosity of solutions at the high extension rates experienced during electrospinning. Finally, dimensional analysis of the model yields a correlation for electrospun fiber diameter in terms of measurable fluid properties, controlled process parameters, and measured jet variables, demonstrating the influence of mechanics in the straight portion of the jet on ultimate fiber morphology.

1. Introduction

Electrospinning has received significant attention as a method to produce nanofibers with varied morphology for a wide range of materials [1]. Potential applications include tissue engineering [2,3], electrical and optical materials [4,5], and multifunctional composites [1]. Examples of electrospinning fluids under investigation include polymer solutions [6–8] and melts [9], polymer–nanoparticle suspensions [10–12], and sol–gel solutions [13]. Despite the variety of materials being electrospun, the process remains essentially unchanged from its conception in the 1930's [14]. In a typical process (Fig. 1), a polymer solution or melt is supplied through a capillary ~10–20 cm above a grounded substrate. The process is driven by an electrical potential of the order of kilovolts applied between the capillary and the substrate. The applied voltage, V, fluid flow rate, Q, and separation distance, H, are manipulated such that a steady, electrostatically driven jet of fluid is drawn from the capillary tip and is collected upon the grounded substrate.

Precise balance of the applied flow rate and voltage can lead to steady electrospinning, where a continuous jet is emitted from the fluid cone at the capillary tip [15]. In steady jetting, a straight portion of the jet occurs close to the fluid cone, where only axisymmetric motion of the jet is observed. This region of the jet remains unchanged in time. However, further along its path the jet can be rendered unstable by non-axisymmetric instabilities such as bending [16] and branching [17], where lateral motion of the jet is observed in the portion near the grounded target.

It has been proposed that the extreme stretching experienced by the jet, due to the non-axisymmetric motion, results in the production of nanoscale fibers [18]. Axisymmetric capillary instabilities have also been shown to produce beading of electrospun fibers [19,20]. However, the role of the straight portion of the jet in determining final fiber morphology has not been well established. The primary focus of this work is to develop both theoretical and empirical understanding of the straight portion of the electrospinning jet, and its relevance to electrospun fiber morphology.

Recent models for electrospinning jets apply electrohydrodynamic (EHD) theory to describe the kinematics of the jet [21]. One class of models typically treats the jet mechanics using the localized-induction approximation by analogy to aerodynamically driven jets [16,22]. These models include the viscoelasticity of the spinning fluid [16,19,23], and have also been augmented to account for solvent evaporation in the jet [22]. While such models have been found to accurately describe the bending instability and give predictions for ultimate fiber morphology, they typically contain several model parameters that cannot be easily

* Corresponding author. Tel.: +1 302 831 8079; fax: +1 302 831 1048.
E-mail address: wagnernj@udel.edu (N.J. Wagner).

0032-3861/$ – see front matter © 2008 Elsevier Ltd. All rights reserved.
doi:10.1016/j.polymer.2008.04.025

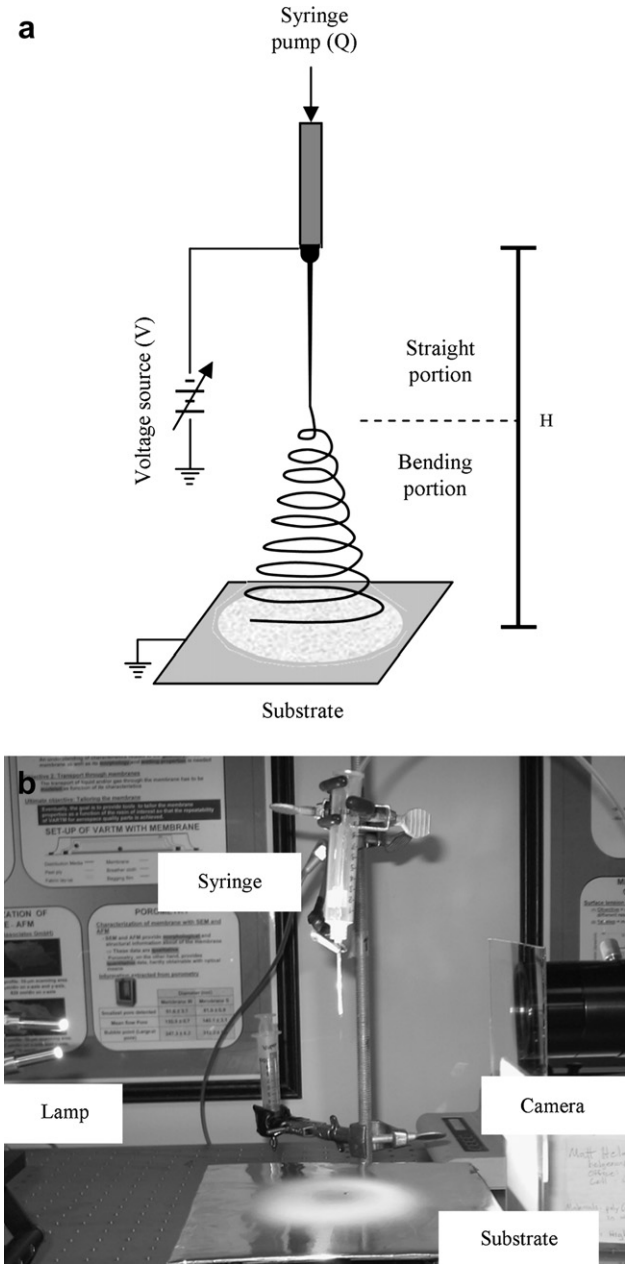

Fig. 1. (a) Diagram of the electrospinning process showing straight and bending portions of the jet. (b) Photograph of apparatus used for electrospinning and high-speed videography measurements.

related to measurable variables. As a result, these models lack predictive capability allowing design and control of the electrospinning process.

In this work, we consider a different class of EHD models that follow the Taylor-Melcher slender body theory described by Saville [21]. Such an approach has led to detailed descriptions of stable jet kinematics for model fluids [9,24,25], which can be predicted using measurable fluid properties and process variables. Stability analysis of these models enables prediction of the onset of bending and capillary instabilities [16,19,23]. Simplifications of these models have led to predictions for the final fiber diameter obtained by electrospinning [16,26], although they show limited applicability across different materials. Although successful for describing the electrospinning of Newtonian fluids these models show limited applicability to non-Newtonian liquids. For example, the operating maps predicted using stability analysis by Hohman et al. [19] are in quantitative agreement with experimentally observed behavior for glycerol, whereas agreement is less convincing for aqueous polymer solutions. Numerical modeling by Feng [25,27] extended the analysis of stable jets to non-Newtonian fluids, showing the importance of the extensional rheology of the spinning fluid. However, such theoretical models typically leave solutions for jet behavior in terms of internal process scales, which are difficult to measure or predict. Thus, a practical understanding of the role of fluid viscoelasticity in determining stable jet mechanics is lacking.

Validating EHD models for electrospinning requires precise measurements of jet kinematics (i.e., jet radius and velocity) which can be directly compared with model predictions. However, due to the small sizes (nm to μm) and high velocities (up to 1 m/s) of the jet, these quantities are challenging to measure accurately, requiring high-speed photography. For example, Reneker et al. [16] showed that the chaotic appearance of electrospinning jets in the unstable region was due to bending of the jet rather than splaying into multiple jets as previously believed. Studies by Hayati [28] involving flow visualization of the jet origin showed relatively mild flows compared to the electrospinning jet itself. Larrondo and Manley [29] were the first to quantitatively measure the jet velocity profile of electrospun polymer melts using particle tracking velocimetry (PTV). Recent work by Bellan et al. uses fluorescent particles in PTV and compares the jet profile to the velocimetry measurements [30]. Similarly, Lopez-Herrera and Ganan-Calvo [31] performed measurements of the capillary breakup process in electrified jets, in part confirming and extending theoretical predictions originally made by Taylor for capillary breakup in the presence of electric fields [32].

The current work focuses on the application of in situ high-speed photography and velocimetry to measure flow kinematics in the straight portion of viscoelastic electrospinning jets. The results are used to test the assumptions and predictions of current theoretical models, similar to what has been done for more traditional fiber drawing processes [33]. Combining such measurements with analytical models in this work leads to the development of a new semi-empirical understanding of the flow of electrospun jets, as well as the development of a novel method for measuring the steady state extensional viscosity of semi-dilute polymer solutions. Furthermore, the measurements identify the role of polymer viscoelasticity in governing the kinematics in the straight portion of the jet, as well as its effect in determining final fiber morphology.

2. Electrohydrodynamic modeling

The mechanics of electrospinning jets are typically modeled using the Taylor-Melcher leaky dielectric model [21]. The electrospinning jet is modeled as a cylindrical fluid element (Fig. 2) of radius R traveling with velocity v_z in the positive z-direction subject to a local electric field E_z over a total path length L. The fluid element has interfacial tension γ, local interfacial charge σ and tensile stress τ. For electrospinning, the slender body assumption is typically invoked, which assumes that the radius of the jet is much smaller than its overall path length ($R \gg L$). Together, these assumptions allow one to write one-dimensional conservation equations for mass, charge and momentum, which in addition to Gauss' Law comprise a closed set of equations to describe the variables R, v_z, E_z, σ, and τ. A general treatment of Taylor-Melcher theory has been developed for stable electrospinning jets by Feng [25,27]. Feng used inherent scales for the process $\{R_0, v_0 = Q/\pi R_0^2, E_0 = I/\pi R_0^2 K = \eta_0 v_0/R_0$, and $\sigma_0 = \bar{\varepsilon} E_0\}$ to cast the equations in a dimensionless form, where $E_0 = V/H$ and R_0 can be determined from jet radius measurements. Here, Q is the volumetric flow rate of material supplied to the jet; K, ρ, ε, and η_0 are, respectively, the conductivity, density, dielectric constant, and zero-shear rate viscosity of the fluid comprising the jet; and $\bar{\varepsilon}$ is the dielectric constant

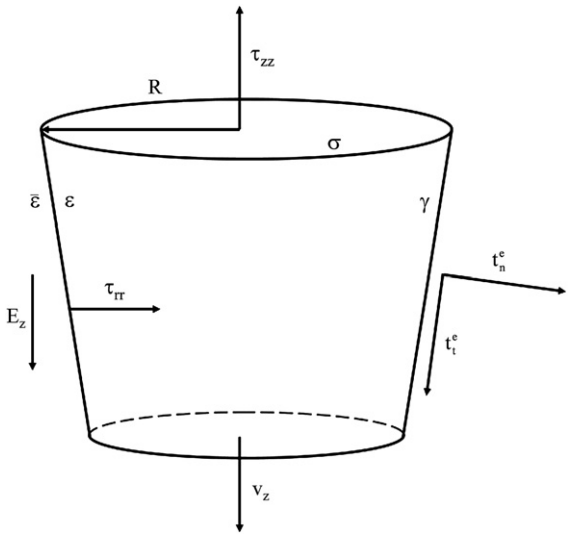

Fig. 2. Schematic of the cylindrical fluid element used in electrohydrodynamic modeling.

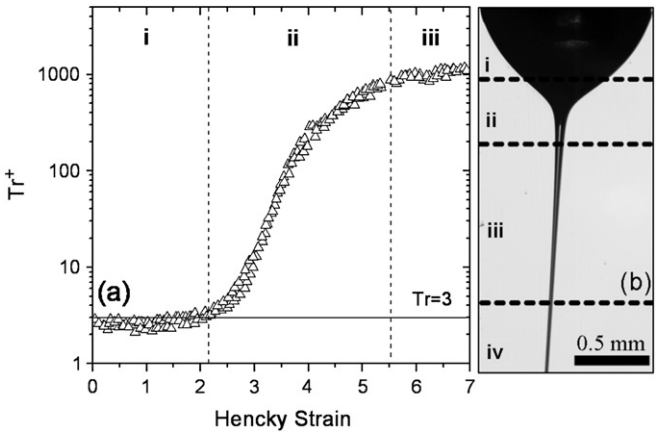

Fig. 3. (a) Trouton ratio versus Hencky strain for a 0.05 wt% solution of polystyrene, MW = 2000 kg/mol (reproduced from Anna et al. [35]). (b) High-speed photograph of an aqueous polyethylene oxide jet showing various flow regimes as determined by jet kinematic measurements.

of the medium surrounding the jet (typically atmosphere). Using these characteristic scales, Feng derived the following dimensionless balance equations (where $\_'$ denotes differentiation along the z-direction):

$$\tilde{R}^2\tilde{v}_z = 1, \tag{1}$$

$$\tilde{R}^2\tilde{E}_z + \mathrm{Pe}_e\tilde{R}\tilde{v}_z\tilde{\sigma} = 1, \tag{2}$$

$$\tilde{v}_z\tilde{v}_z' = \frac{1}{\mathrm{Fr}} + \frac{\tilde{T}'}{\mathrm{Re}_j\tilde{R}^2} + \frac{1}{\mathrm{We}}\frac{\tilde{R}'}{\tilde{R}^2} + \varepsilon\left(\tilde{\sigma}\tilde{\sigma}' + \beta\tilde{E}_z\tilde{E}_z' + \frac{2\tilde{\sigma}\tilde{E}_z}{\tilde{R}}\right), \tag{3}$$

$$\tilde{E}_z = \tilde{E}_0 - \ln\chi\left[\left(\tilde{\sigma}\tilde{R}\right)' - \frac{\beta}{2}\left(\tilde{E}\tilde{R}^2\right)''\right], \tag{4}$$

where $\beta = (\varepsilon/\bar{\varepsilon}) - 1$ and χ is the aspect ratio, R/L, of the jet. The dimensionless groups defined in the original work [25], are: Pe_e, the electrical Peclet number as a ratio of the characteristic time for flow to that for electrical conduction; Fr, the Froude number relating inertial to gravitational forces; Re_j, the Reynolds number as a ratio of fluid inertial to viscous forces; We, the Weber number as a ratio of inertial to surface tension forces; and ε, the electrostatic stress relative to the kinetic energy of the jet. Typical values of these dimensionless groups based on kinematic measurements for electrospinning of a 4 wt% aqueous polyethylene oxide solution are given in Table 1.

The dimensionless tensile stress, $\tilde{T} = \tilde{R}^2(\tilde{\tau}_{zz} - \tilde{\tau}_{rr})$, in Eq. (3) requires an appropriate constitutive relation to close the equations, along with boundary conditions for the velocity, stress field and jet radius. In general, $\tilde{T}$ will depend on the total accumulated strain on the jet as well as the instantaneous strain rate, $\tilde{v}_z'$. The bracketed term in Eq. (3) is the electromechanical stress (EMS) on the fluid due to the electrical field, and is comprised of two components [25], the surface normal electrostatic traction $\tilde{t}_n^e = \varepsilon(\tilde{\sigma}\tilde{\sigma}' + \beta\tilde{E}_z\tilde{E}_z')$ and the surface tangent electrostatic traction $\tilde{t}_n^e = 2\varepsilon\tilde{\sigma}\tilde{E}_z/\tilde{R}$, as shown in Fig. 2.

Feng solved Eqs. (1)–(4) under various applied fields and fluid properties [27], particularly for non-Newtonian fluids with extensional thinning, thickening, and strain hardening [27]. Here, we develop a simplified understanding of electrospinning jets based on the evolution of the tensile stress due to elongation, which are expected to follow the behavior typically observed during uniaxial extension of a polymeric fluid [34]. Most entangled polymer solutions and melts exhibit strain hardening, whereby the transient extensional viscosity, η_e^+, increases rapidly with the applied strain. The qualitative features typically associated with strain hardening are depicted in Fig. 3a for a model polymer solution [35], where the transient Trouton ratio, $\mathrm{Tr}^+ = \eta_e^+/\eta_0$, is plotted versus the extensional strain (or Hencky strain). At low strain, the extensional viscosity is roughly equal to that expected for a Newtonian fluid ($\eta_e^+ = 3\eta_0$), such that Tr = 3. As the strain is increased, the Trouton ratio increases by as much as several orders of magnitude, and eventually limits at larger strains to a plateau Tr_∞^+, which depends on the applied strain rate [34]. Thus, for uniaxial extension of a jet of polymer fluid, three flow regimes are defined under the assumption of uniaxial extension for the kinematics of the electrospun jet: (I) pseudo-Newtonian behavior at low strains, (II) strain hardening marked by a significant increase in the extensional viscosity, and (III) pseudo-steady extension where $\eta_e^+ = \eta_{e,\infty}^+$.

Fig. 3b shows a high-speed photograph of the straight portion of an electrospinning jet identifying these flow regimes. The jet originates from a fluid cone just after the orifice [32,36]. Particle tracking velocimetry measurements by Hayati [28] show little extensional deformation of the spinning fluid in the cone region [region (i) in Fig. 3a]. At the origin of the jet, there is significant extensional flow as the jet is drawn by the electromechanical stress. Calculations by Feng show a rapid increase in the tensile stress in

Table 1
Typical values of dimensionless groups in EHD modeling

	4 wt% PEO				
Applied voltage:	5.1 kV	5.7 kV	6.0 kV	6.7 kV	7.0 kV
$\mathrm{Pe}_e = 2\varepsilon v_0/KR_0$	1.3×10^{-7}	2.2×10^{-7}	2.3×10^{-7}	2.7×10^{-7}	2.2×10^{-7}
$\mathrm{Fr} = v_0^2/gR_0$	8.6×10^{-4}	2.4×10^{-3}	3.1×10^{-3}	4.3×10^{-3}	3.5×10^{-3}
$\mathrm{Re}_j = \rho v_0 R_0/\eta_0$	5.8×10^{-5}	1.1×10^{-4}	1.5×10^{-4}	1.9×10^{-4}	2.0×10^{-4}
$\mathrm{We} = \rho v_0^2 R_0/\gamma$	2.2×10^{-6}	7.1×10^{-6}	1.1×10^{-5}	1.8×10^{-5}	1.8×10^{-5}
$\varepsilon = (\varepsilon-\bar{\varepsilon})E_0^2/\rho v_0^2$	19.2	8.8	7.2	5.7	7.1

this region, in accordance with strain hardening behavior [region (ii)]. After some distance, the tensile stress on the jet ceases to increase [27], indicating the onset of pseudo-steady extensional stretching of the electrospinning jet [region (iii)]. As the jet continues to accelerate and thin, the extensional stress on the jet becomes negligible with respect to the jet inertia and EMS [region (iv)] [25,37]. Identifying these limiting flow regimes allows for simplification of the EHD model given by Eqs. (1)–(4). In the following, we discuss these simplifications for each of the flow regimes depicted in Fig. 3, and, where applicable, identify experimentally verifiable scaling relationships for the kinematics of electrospinning jets.

2.1. Fluid cone

The morphology and stability of suspended fluid drops subjected to strong electric fields were studied by Taylor [32], who found a self-similar conical shape, henceforth referred to as the Taylor cone. More recent work by Yarin et al. [36] has shown that the Taylor cone is only one particular self-similar shape for the pendant drop, and establishes more rigorous stability criteria applicable to non-Newtonian fluids, as well as estimates for the initial jet radius. The instability of the Taylor cone leads to jet formation, where the jet emanates from a residual fluid cone. This residual fluid cone exhibits three-dimensional flows not captured by slender body theory [28], and as such no simple scaling predictions for R or v_z can be obtained using the current framework.

2.2. Jet initiation

Jetting from the fluid cone is characterized by a rapid decrease in radius coinciding with a large increase in magnitude of the local electric field, such that the polarization contribution of the normal electrostatic traction, $\beta\tilde{E}_z\tilde{E}'_z$, dominates the EMS [25]. The resulting increase in EMS on the jet is resisted by rapid strain hardening of the spinning fluid. Thus, the jet current is dominated by charge conduction, and jet motion is governed by the balance of the polarization contribution of the EMS with the tensile stress on the fluid. In this limit, Eqs. (2) and (3) become:

$$\tilde{R}^2\tilde{E}_z = 1 \tag{2-ii}$$

$$\frac{\tilde{T}'}{\mathrm{Re}_j\tilde{R}^2} + \varepsilon\beta\tilde{E}_z\tilde{E}'_z = 0. \tag{3-ii}$$

Here, jet inertia, gravity, and surface tension are neglected in the momentum equation, which is justified by the very small values of Re_j, Fr, and We at the jet origin (see Table 1). Also neglected is the contribution of free charge to the EMS, which has been experimentally verified near the jet origin for non-ionic polymeric fluids [38]. The axial distance over which region (ii) persists can be inferred from the transient extensional behavior of the fluid. It should be noted that Eq. (3-ii) and the assumptions leading to it are a novel simplification of the jet mechanics relevant to spinning of viscoelastic polymer solutions.

2.3. Jet stretching

Steady state extension (where $\eta_e^+ = \eta_{e,\infty}^+$) of polymeric fluids is typically reached after several strain units [39], where the extensional strain is defined by the Hencky strain $\varepsilon = \ln(R/R_0)$. For the electrospinning jet, this corresponds to z-distances of several times R_0. Because $\eta_{e,\infty}^+$ depends only on the extension rate the fluid can be modeled in the jet stretching region as a generalized Newtonian fluid with the following constitutive equation [34]:

$$\tilde{T} = \mathrm{Tr}_\infty^+\left(\tilde{R}^2\tilde{v}'_z\right). \tag{5}$$

Substituting Eq. (5) into Eq. (3-ii) yields,

$$\frac{\left(\tilde{R}^2\tilde{v}'_z\right)'}{\tilde{R}^2} + \Pi_\infty\tilde{E}_z\tilde{E}'_z = 0, \tag{3-iii}$$

where, $\Pi_\infty = \varepsilon\beta\mathrm{Re}_j/\mathrm{Tr}_\infty^+ = (\varepsilon-\bar{\varepsilon})E_0^2R_0^3/\pi\eta_{e,\infty}^+Q$.

The dimensionless group Π_∞ governs jet dynamics in the jet stretching regime. Substituting Eqs. (1) and (2-ii) to eliminate $\tilde{v}_z = \tilde{R}^{-2}$ and $\tilde{E}_z = \tilde{R}^{-2}$, respectively, in Eq. (3-iii) allows one to solve the jet kinematics using two boundary conditions. Integrating Eq. (3-iii) once yields:

$$\tilde{R}^2\tilde{v}'_z + \Pi_\infty\tilde{E}_z = A,$$

where A is a constant of integration. Physical reasoning suggests $A=0$, because under zero applied electric field Π_∞ and $\tilde{v}'_z$ must be zero. The second boundary condition is that at the initial point of jet stretching, $\tilde{z}_{\mathrm{iii}}$, the jet initiates from vanishing velocity, such that $\tilde{v}(\tilde{z}_{\mathrm{iii}}) = 0$. Integrating Eq. (3-iii) once more and applying this boundary condition yields:

$$\tilde{R} = [\Pi_\infty(\tilde{z}-\tilde{z}_{\mathrm{iii}})]^{-1/2}, \text{ and } \tilde{v}_z = \Pi_\infty(\tilde{z}-\tilde{z}_{\mathrm{iii}}). \tag{6}$$

Thus, in the jet stretching regime the EHD model predicts a power law scaling of the jet kinematics. Furthermore, we note that the instantaneous extension rate, $\dot{\varepsilon} = \tilde{v}'_z$, is a constant and directly proportional to the dimensionless group Π_∞.

It should be noted that the assumptions leading to Eq. (6), which are based on analogy to uniaxial extensional flow, are distinctly different than those used in previous analyses. A similar scaling of $R \sim z^{-1/2}$ was derived previously by He et al. [40] using the electrospinning model developed by Spivak and Dzenis [24]. However, it has been previously acknowledged that several key terms are absent in the Spivak and Dzenis model [27], including the normal EMS, and their assumption of negligible viscous contributions to the jet momentum is most likely invalid given the previous discussion. Similarly, Rutledge and Fridrikh predict a different scaling of $R \sim z^{-1}$ in the jet stretching regime [41], which contradicts experimental measurements on jets comprised of Boger fluids exhibiting a scaling of $R \sim z^{-1/2}$ in the appropriate region [39]. Thus, the current analysis is the first prediction of the experimentally observed $R \sim z^{-1/2}$ scaling arising from the balance of electromechanical and viscoelastic stresses arising from strain hardening of the electrospinning fluid.

2.4. Jet thinning

At significantly high Hencky strains, the electric field decreases slowly from its maximum at the jet origin toward the far-field value $E_0 = V/H$. In this region, the surface normal electrostatic traction vanishes, and the jet current is dominated by charge convection rather than conduction. Thus, jet kinematics are dominated by jet inertia and the tangential electrostatic traction. As shown originally by Kirichenko et al. [37] for an inviscid jet and generalized by Feng [25] for non-Newtonian jets, this leads to jet kinematics that scale as $R \sim z^{-1/4}$ and $v_z \sim z^{-1/2}$. In Eq. (3), this is obtained by neglecting all terms except for the jet inertia and tangential EMS.

3. Experimental

3.1. Materials

Aqueous solutions of polyethylene oxide (PEO, MW = 9×10^5 g/mol, Scientific Polymer Products) were prepared by diluting a stock

solution of 6 wt% PEO in deionized water (18.3 MΩ resistivity) following an earlier procedure [12]. Dilutions to 4 wt% and 2 wt% were prepared, along with a 2 wt% PEO solution containing 1 mM NaCl (Aldrich Chemical). For PTV measurements, each solution was seeded with approximately 500 ppm of polyurethane tracer particles (Degussa Chemical) with a nominal diameter of 3 μm. The particles were added in the appropriate amount after each solution was prepared, and the solutions were placed on a roll mixture to ensure complete dispersion of the particles.

3.2. Solution characterization

The zero-shear rate viscosity, η_0, and the relaxation time, λ, of the PEO solutions were measured at 25 °C using steady and oscillatory shear measurements, respectively, on a TA Instruments AR-G2 rheometer with a 60 mm 1° cone and plate upper measurement geometry and a lower Peltier heating plate, yielding results comparable to previous studies [42]. The DC conductivity of each solution was measured using a conductivity probe. The tracer particles did not measurably alter the electrostatic and rheological properties of the PEO solutions at the concentrations used. The measured properties of each solution are listed in Table 2.

3.3. Electrospinning and high-speed videography

The electrospinning apparatus shown in Fig. 1b consists of an 18-guage syringe needle connected to the positive lead of a power supply (Gamma High Voltage ES30P) and suspended 10 cm above a grounded aluminum foil target. The solution feed rate is controlled by a syringe pump (Harvard Apparatus HA2000). All experiments were performed under steady state conditions. A high-speed camera (Redlake HG-100 K) protected by an electrically insulating glass plate images the initial portion of the jet at a rate of 2000 fps with a resolution of 672×1128 pixels. The jet is backlit using a fiber-optic halogen source (Fiber-Lite MH-100). All experiments were performed under ambient conditions (~25 °C). Steady state experiments were performed and recorded for all polymer solutions at the process conditions listed in Table 2.

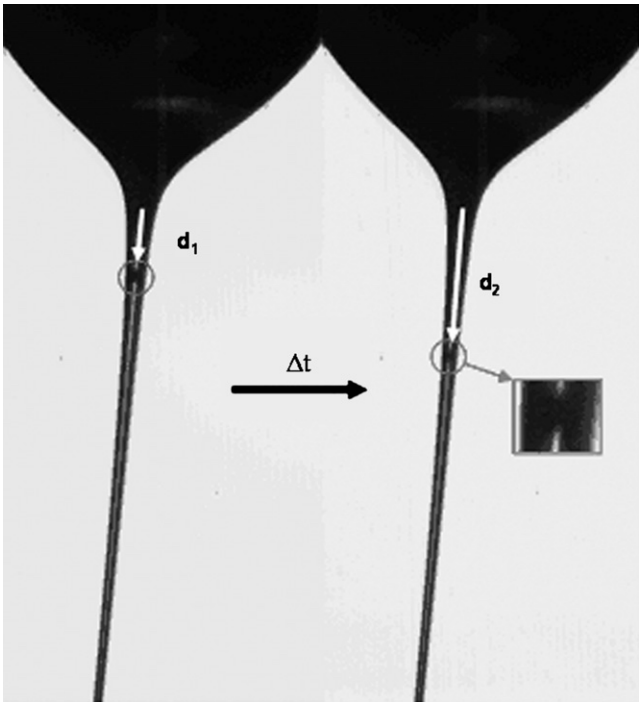

Fig. 4. Representative images (taken 5 ms apart) of a 2 wt% PEO jet electrospun at 5.1 kV and 0.2 mL h, showing a particle (circled) used for PTV measurements. Inset shows enlarged view of tracer particle.

3.4. Image analysis

Jet radius profiles, $R(z)$, are extracted from HSP images using a method described previously [43]. Data are averaged over 20 images for each set of operating conditions to ensure measurement precision. Similarly, jet velocity profiles, $v_{(z)}$, are determined from tracking particle motion via differencing images such as those shown in Fig. 4 using the MotionXtra software package. The measurements are averaged over 10 particle trajectories to obtain sufficient statistical significance. In all cases, data averaging was

Table 2
Summary of experimental conditions and measured solution and fiber properties

PEO concentration (wt%)	NaCl concentration (mM)	η_0 (Pa s)	λ (s)	K (μS/cm)	V (kV)	Q (μL/h)	Dry fiber diameter (nm)	Fiber morphology
2	0	0.11	1.5×10^{-5}[a]	6.90	5.1	200	–	Beads
					5.7	220	–	Beads
					6.0	300	–	Wet beads
					6.7	350	–	Wet beads
					7.0	550	–	Wet film
	1	0.12	1.6×10^{-5}[a]	125	4.6	800	–	Beads
					5.0	1000	93 ± 28	Fibers/beads
					5.5	1250	92 ± 27	Fibers/beads
					6.0	1500	82 ± 27	Fibers
					6.8	2500	84 ± 23	Fibers
4	0	2.67	3.7×10^{-3}	10.3	5.1	25	91 ± 40	Fibers/beads
					6.0	50	165 ± 63	Fibers
					6.5	75	123 ± 12	Fibers
					7.0	100	–	Fibers
					7.5	125	–	Wet film
6	0	15.57	2.2×10^{-2}	12.8	6.1	10	337 ± 49	Fibers/beads
					7.2	20	294 ± 18	Fibers
					7.5	20	259 ± 42	Fibers
					8.8	25	224 ± 31	Fibers
					9.1	30	236 ± 56	Fibers

[a] Too small to measure, estimated using time–concentration superposition [42].

performed over a period of several minutes to ensure the jet profiles were steady in time.

3.5. Fiber characterization

Electrospun PEO fibers and tracer particles are imaged using a JEOL JSM7400F field emission scanning electron microscope (FESEM). Fiber samples are prepared by cutting a sample of the aluminum foil target and adhering it to a specimen stub with carbon tape. Fiber specimens are sputter coated with an Au/Pd film for 40 s (resulting in a film thickness of approximately 10 Å) before imaging. The fiber diameter is measured manually from the micrographs using a statistically significant sampling ($\sim$100).

4. Results

4.1. Jet radius profile

A typical jet radius profile is shown in Fig. 5, where the error bars are characteristic of measurement uncertainty and variation across replicate measurements. The measured jet radius profiles for all PEO concentrations and electrospinning conditions are plotted in Fig. 6. All jet profiles show the same qualitative behavior, regardless of the polymer concentration or applied electrospinning conditions. Namely an initial region of positive curvature ($d^2R/dz^2 > 0$) indicative of the fluid cone, is followed by a significant decrease in radius, marking the origin of the electrospun jet. The jet radius, R_0, at the jet origin, z_{ii}, is defined by the inflection point of $R(z)$ where $d^2R/dz^2 = 0$. The profiles follow the power law scaling predicted by the flow regime model; namely, $R \sim z^{-1/2}$ for the jet stretching region and $R \sim z^{-1/4}$ for the jet thinning region. The latter scaling is not fully evident in the measurement window for all process conditions for the more concentrated solutions, where the jet development requires a longer distance. Based on the derived scaling relationships, we use the following empirical relationship to model the radial jet profile:

$$R(z) = Az^{-n} + Bz^{-1/2} + Cz^{-1/4},\ z > z_{ii}. \quad (7)$$

The first term in Eq. (7) accounts for the initial reduction in radius in the jet initiation region, whereas the last two terms reflect the theoretically predicted behavior for the jet stretching and jet thinning regions, respectively. Because the jet initiation is expected to depend on the extensional viscosity of the spinning fluid, the exponent n is expected to vary with the spinning solution and process conditions. A representative data fit is given in Fig. 5, where exponents in the range of 4–8 are observed (Table 3). The position, z_{iii}, of the onset of the jet stretching regime relative to z_{ii} is taken to be where Eq. (7) with where $A = 0$ describes the data to within 1% error. This is also shown in Table 3. The jet profile parameters are observed to depend systematically on the spinning conditions and solution composition.

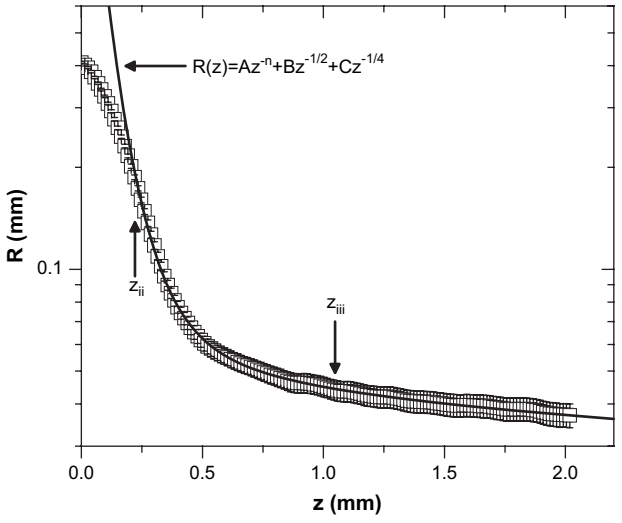

Fig. 5. Jet radius profile for a 2 wt% PEO jet electrospun at 7.0 kV and 550 μL/h. Points represent measured data and the line represents empirical fit to Eq. (7) for the data above the point of jet initiation (marked). Error bars represent variation between images as well as pixel resolution of the CCD camera.

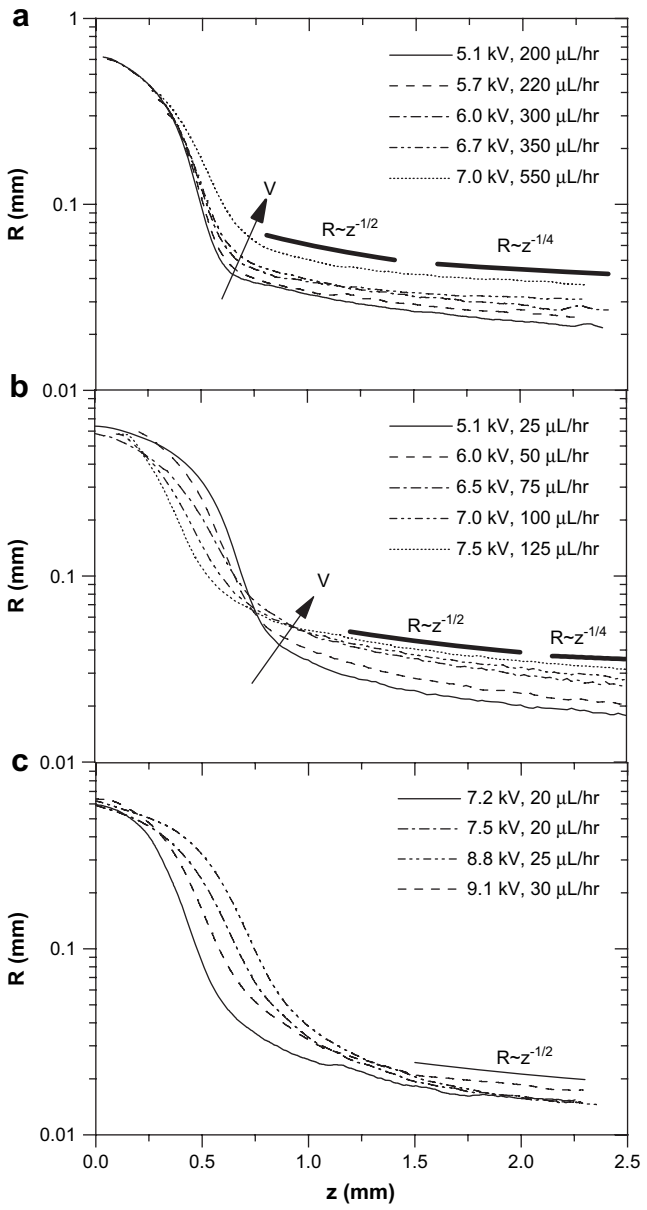

Fig. 6. Jet radius profiles versus axial jet coordinate measured for (a) 2 wt%, (b) 4 wt%, and (c) 6 wt% PEO for the applied voltages and solution flow rates indicated (error bars not shown for visual clarity). Power law behavior predicted by scaling theory is shown for comparison.

4.2. Jet velocity profile

PTV measurements of jet velocity profiles are shown for the 2 wt%, 4 wt%, and 6 wt% PEO solutions at the various experimental conditions in Fig. 7, and all exhibit similar shape. After an initial region of acceleration, the jet velocities reach a region of roughly linear growth, in agreement with theoretically predicted scaling of $v_z \sim z^1$ for jet stretching. This is followed by a region where $v_z \sim z^{1/2}$, in agreement with the prediction jet thinning.

Table 3
Stable jet flow kinematic parameters[a]

PEO concentration (wt%)	NaCl concentration (mM)	V (kV)	R_0 (mm)	z_{iii} (mm)	n
2	0	5.1	0.289	0.540	8.0
		5.7	0.285	0.572	8.0
		6.0	0.268	0.600	6.8
		6.7	0.275	0.778	5.5
		7.0	0.292	0.792	5.4
	1	4.6	0.221	0.576	16.2
		5.0	0.150	0.564	15.3
		5.5	0.148	0.610	14.1
		6.0	0.149	0.633	12.4
		6.8	0.159	0.734	7.2
4	0	5.1	0.222	1.127	7.0
		6.0	0.180	1.227	5.3
		6.5	0.141	1.177	4.4
		7.0	0.138	1.181	4.0
		7.5	0.109	1.127	4.5
6	0	6.1	0.344	1.413	3.8
		7.2	0.278	1.355	4.0
		7.5	0.2564	1.3026	4.4
		8.8	0.2224	1.3021	4.6
		9.1	0.3138	1.3826	3.9

[a] Obtained by fitting $R(z)$ to Eq. (7) as described in the text.

The PTV measurements also enable quantitative evaluation of assumptions underlying the EHD model, namely slender body behavior and negligible mass transfer (by solvent evaporation) in the straight portion of the jet, which lead to plug flow kinematics. Rearrangement of Eq. (1) yields

$$v(z) = \frac{Q}{\pi R(z)^2}. \tag{8}$$

Eq. (8) relates the jet velocity profiles to the radial jet profiles, $R(z)$. As shown in Fig. 7 the velocity profiles calculated from Eq. (8) are in quantitative agreement with those measured by PTV, thus confirming the slender body assumption for the stable PEO jets.

It is useful to define a metric of the velocity profile to compare across different experimental conditions as well as known rheological behavior of the PEO solutions. Here, it is natural to use the effective extension rate during jet stretching, $\dot{\varepsilon}_{iii}$, which is calculated as the slope of the linear portion of the velocity profile (in units of 1 s^{-1}) and plotted in Fig. 8. The extension rate increases approximately linearly with the applied voltage, as expected theoretically from Eq. (6), where proportionality between $\dot{\varepsilon}_{iii}$ and Π_∞ is predicted. In general, the magnitude of $\dot{\varepsilon}_{iii}$, as well as its overall dependence on applied voltage, decreases as the concentration of PEO increases, i.e. as the spinning solution becomes more viscoelastic.

4.3. Fiber morphology

Representative micrographs of electrospun materials are shown in Fig. 9, and average fiber diameters and fiber morphologies are summarized in Table 2. The fiber diameter increases with increasing PEO concentration, in agreement with previous reports [12,20,44]. Increasing the PEO concentration from 2 wt% to 6 wt% leads to a transition from beaded to smooth fibers. Finally, where continuous fibers without beads are observed, the fiber diameter decreases as the applied voltage increases. Fibers containing beads are smaller than continuous fibers spun at the same PEO concentration, which is due to capillary breakup [45].

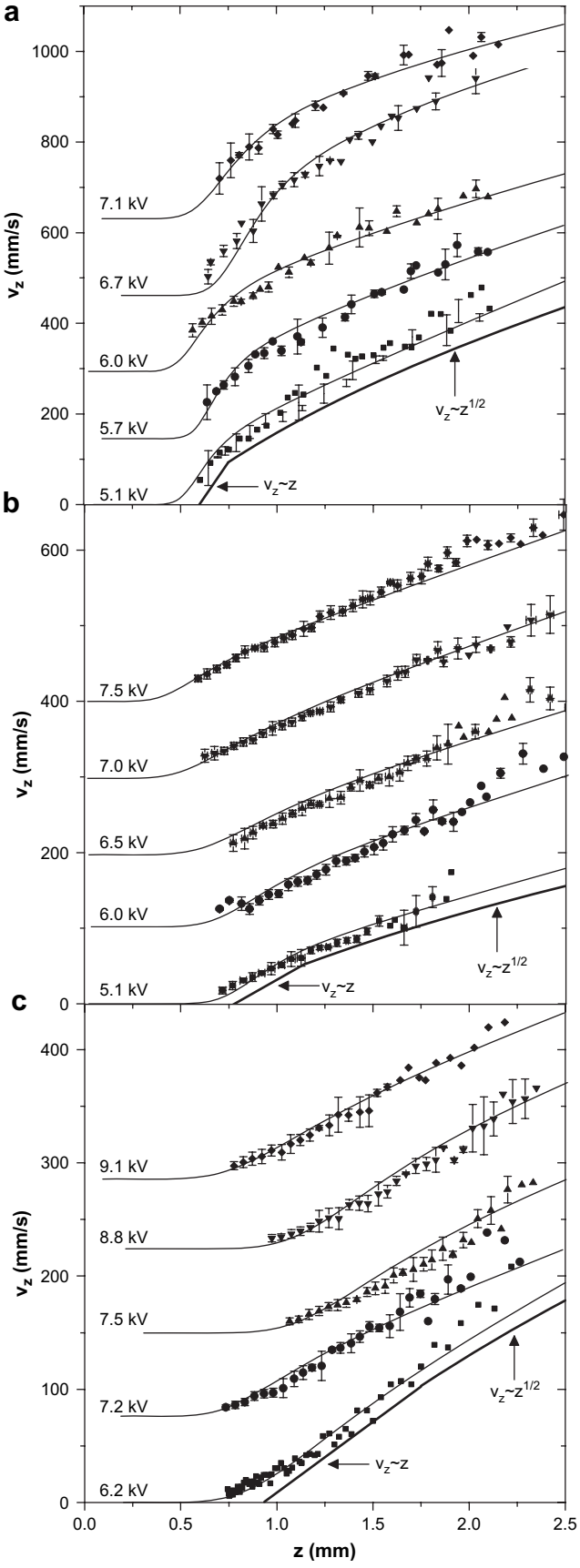

Fig. 7. Jet velocity profiles for electrospinning of (a) 2 wt%, (b) 4 wt%, (c) 6 wt% PEO at the applied voltages indicated. Points represent data measured by PTV, whereas lines represent theoretical profiles predicted from profiler(z) using Eq. (8). The data have been vertically shifted for visual clarity.

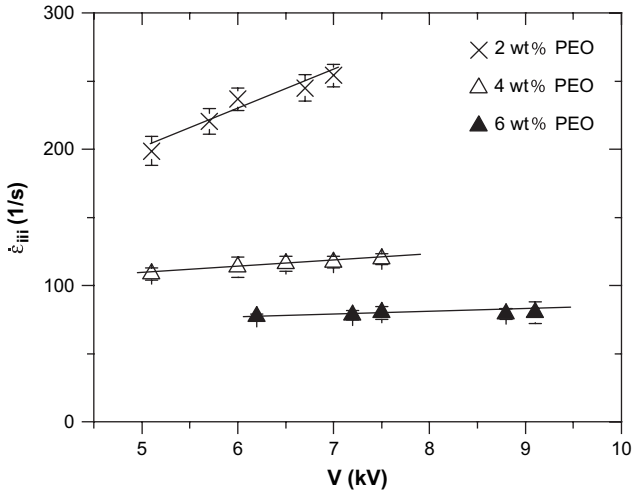

Fig. 8. Jet stretching extension rate versus applied voltage measured by PTV for the PEO concentrations indicated. Lines are given to guide the eye.

Polymer solution elasticity also has been shown to determine the final morphology of electrospun fibers by suppressing capillary instabilities [39,46]. Here, the 2 wt% solution, which is below the entanglement concentration c_e [42], has insufficient elasticity to dampen capillary disturbances, resulting in beaded fibers. However, continuous fibers that contain relatively few beads are observed above c_e at 4 wt%, while even fewer beads are observed at 6 wt%.

4.4. Electrospinning of PEO–NaCl solutions

The addition of charged species, such as salts or polyelectrolytes, to the spinning solution suppresses the capillary instability and produces larger diameter fibers [20]. These results are consistent with theoretical predictions by Hohman et al. [23], who showed that the onset and growth rate of both the bending and capillary instabilities depend on the solution's conductivity. However, less is known about the effects of increasing the solution's conductivity on the straight portion of the jet considered here. In the EHD model, increasing the ion concentration increases the tangential electrostatic traction on the jet. As this term was neglected in the scaling analysis of the current work, it is unclear *a priori* whether solutions with high conductivity should be expected to follow the relationships derived for regions (ii–iv). To test this, measurements were performed on a solution containing 2 wt% PEO containing 1 mM NaCl, under conditions summarized in Table 2. Rheological measurements summarized in Table 2 show that the viscoelasticity is not significantly influenced by the addition of NaCl, whereas the conductivity increases by 20-fold.

Fig. 10 shows jet radius profiles for the PEO–NaCl, solution which are similar to that for the 2 wt% PEO solution in Fig. 5. Closer inspection shows that the jet thinning regime (where $R \sim z^{-1/4}$) is no longer evident in the experimental window, and the jet radius is thinner. Using Eq. (8), the parameters R_0, z_{iii}, and n were determined and are shown in Table 3. A significant decrease in R_0 is observed upon addition of salt, accompanied by an increase in the strain hardening exponent n to nearly double the value obtained for similar solutions without added NaCl. The profile in region (iii) was fit in order to obtain jet stretching extension rates for solutions containing NaCl (Fig. 11), which exhibit a 3-fold increase in extension rate upon addition of NaCl. This suggests that the addition of electrolyte significantly increases the electromechanical stress on the electrospun jets, leading to stronger jet thinning and extension in regions (ii) and (iii). However, the general features of the jet kinematic profiles predicted by the EHD model are preserved upon salt addition.

Fig. 9 shows representative images of electrospun material obtained from the PEO–NaCl solutions showing significant bead formation at low voltages. With increasing voltage a transition to beaded fibers and eventually continuous fibers of less than 100 nm is observed. As fibers are never observed under the same process conditions without added salt, the occurrence of continuous fibers here can be attributed to changes in electrical properties of the PEO solution upon addition of NaCl. This effect has been previously observed for PEO solutions containing added salts including NaCl [47].

5. Analysis and discussion

5.1. Jet kinematics and extensional rheology

The success of the one-dimensional slender body EHD model in characterizing the jet kinematics suggests that all of the PEO jets studied exhibit a self-similar kinematic profile in the stable portion that is described by the limiting features of the flow regime model, namely: (i) the fluid cone noted by positive curvature of the jet radius profile, (ii) jet initiation marked by a significant decrease in jet radius with scaling exponents in the range of $R \sim z^{-n}$, (iii) jet stretching in which the jet radius and velocity scale with $R \sim z^{-1/2}$ and $v \sim z^{1}$, and (iv) jet thinning in which the jet radius and velocity scale with $R \sim z^{-1/4}$ and $v \sim z^{1/2}$.

As the behavior of regions (ii) and (iii) are dominated by the extensional response of the fluid, the trends in electrospinning kinematics can be understood by considering the extensional rheology and strain hardening of the polymer solutions. For example, in uniaxial extension the tensile stress should be related to the extension rate by $T = \eta^{+}_{e,\infty}\dot{\varepsilon}$. According to Eq. (3-iii), this stress is balanced by the electromechanical stress. Thus an increase in extensional viscosity at a given applied EMS (or voltage) should result in a decrease in the jet extension rate. Similarly, an increase in the applied EMS (by increasing the applied voltage) should result in an increase in the jet extension rate. Both of these expected trends are observed in the data presented in Fig. 8, where $\dot{\varepsilon}_{iii}$ is shown to increase with increasing applied voltage and decrease with increasing polymer concentration (extensional viscosity).

The variation in the jet initiation exponent n also follows the expected trends in the extensional viscosity and strain hardening of the PEO solutions, as follows. Increased viscoelasticity and extension rates result in a more pronounced strain hardening response. This more pronounced strain hardening serves to resist the thinning of the jet in region (ii), yielding a lower value of the thinning exponent n. Feng modeled this effect for polymeric liquids in greater detail with similar results [25].

Feng's calculations [27] applied to Giesekus fluids also show that the onset of steady state extensional behavior, corresponding to z_{iii} in our analysis, is set by the Deborah number, $De = \lambda\dot{\varepsilon}$, such that z_{iii} increases with increasing *De*. In general, the experimentally determined values of z_{iii} qualitatively agree with this finding, where z_{iii} increases relative to R_0 with increasing values of λ for the PEO solutions as well as increasing values of $\dot{\varepsilon}_{iii}$ measured using PTV. These trends in electrospinning behavior do not change upon salt addition because salt addition does not significantly affect the rheology of the PEO solutions.

Overall, these results suggest that the parameters $\dot{\varepsilon}_{iii}$, n, and z_{iii} can be used as simple metrics of the strain hardening of electrospinning jets that can be compared across multiple fluids and process conditions, as well as to direct rheological measurements of extensional strain hardening, similar to what has previously been done for melt spinning processes [48]. Further quantification of the effects of extensional rheology on stable electrospinning requires

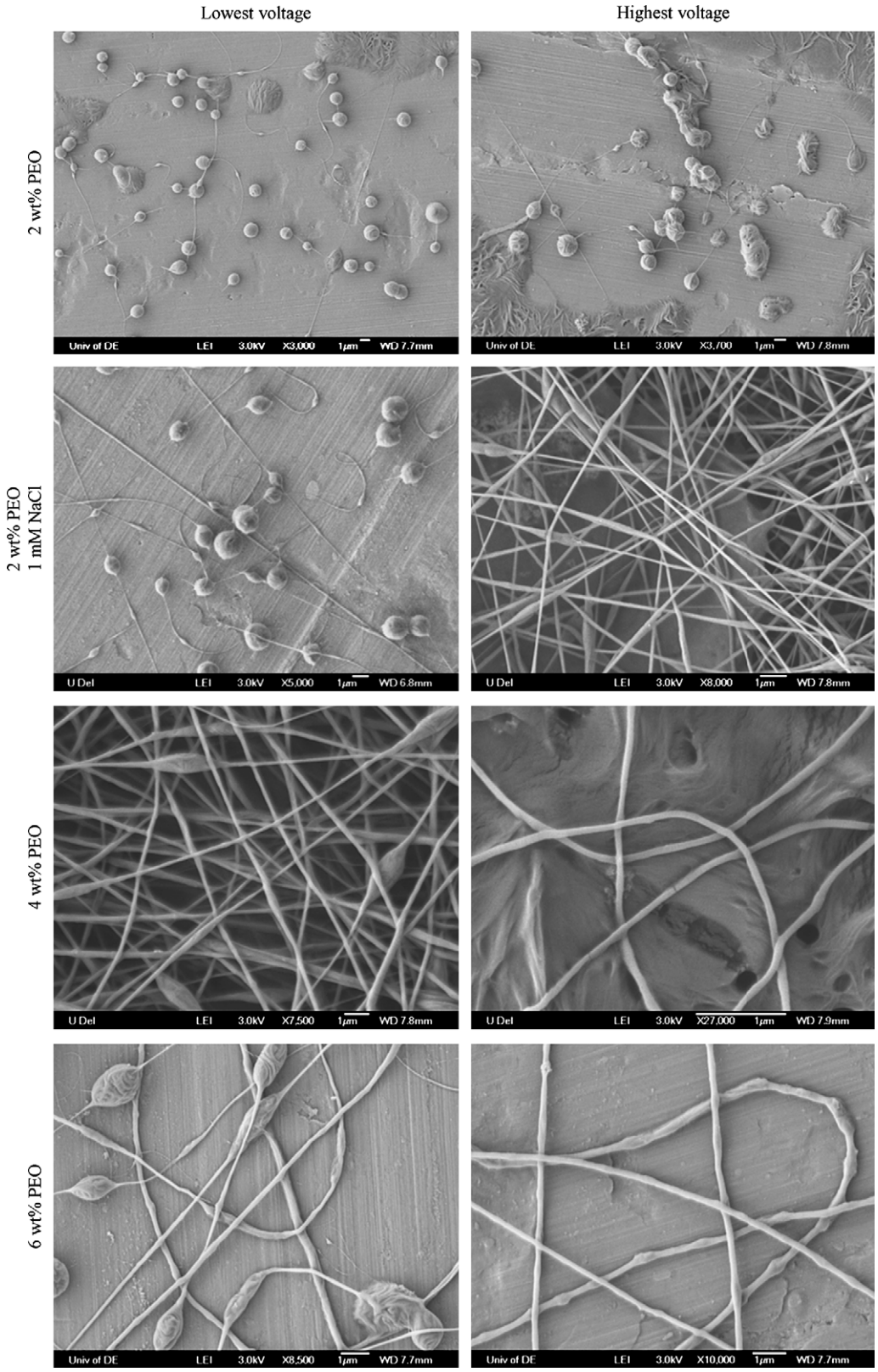

Fig. 9. FESEM micrographs of electrospun PEO fibers at the concentrations shown for the lowest and highest applied voltages. Scale bars are all 1 μm.

measurement of extensional viscosities at the rates relevant to electrospinning. Unfortunately, current experimental capabilities only allow determination of uniaxial extensional properties up to extension rates around $10\,s^{-1}$ [49]. However, because the kinematics of the jet stretching region correspond to steady state uniaxial extension, the kinematic measurements allow estimation of the steady state extensional viscosity of the spinning fluid. Rearranging Eq. (6) using the definition of Π_∞, we obtain the following expression for the *apparent steady state extensional viscosity* of the spinning fluid in region (iii):

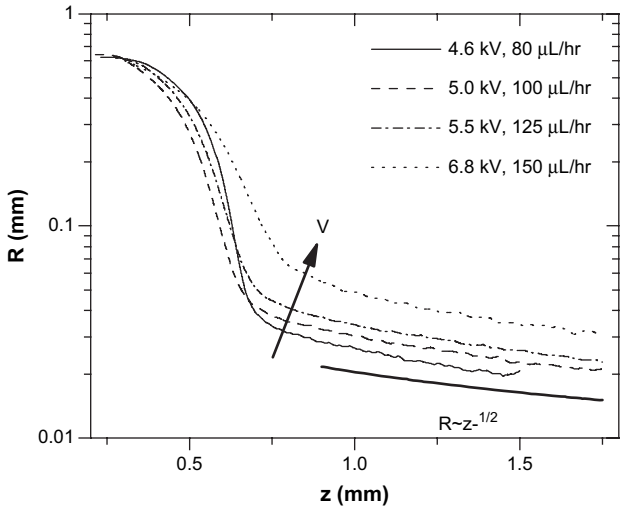

Fig. 10. Jet radius profiles versus axial jet coordinate measured for 2 wt% PEO with 1 mM NaCl for the conditions indicated. Power law behavior predicted for jet stretching is shown for comparison.

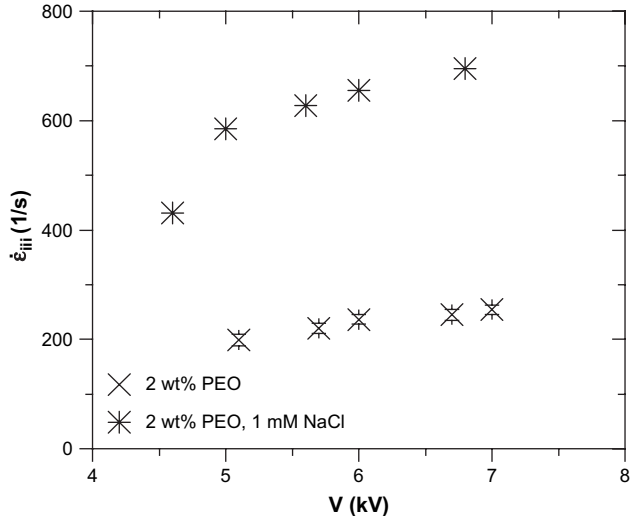

Fig. 11. Jet stretching extension rate for 2 wt% PEO with and without 1 mM NaCl.

$$\overline{\eta}_{e,app} = \frac{(\varepsilon - \overline{\varepsilon})E_0^2 R_0^2 v_0}{\pi Q \dot{\varepsilon}_{iii}}. \quad (9)$$

Thus, the steady state extensional viscosity can be determined from the dielectric properties of the fluid and surroundings, controlled process parameters, and measured jet kinematics. Note that the extension rates exceed 100 s^{-1}, which is well above what can be measured by filament stretching. The apparent extensional viscosities calculated from Eq. (9) are shown in Fig. 12, along with the expectation for a Newtonian fluid ($\eta_e = 3\eta_0$), which are calculated from shear viscosity measurements [42] and are independent of extension rate. Below c_e the extensional viscosity is in quantitative agreement with that expected for a Newtonian fluid and no appreciable strain hardening is observed. For concentrations above c_e, the apparent extensional viscosity significantly exceeds that expected for a Newtonian fluid, which is consistent with entanglement at these higher concentrations. For the 6 wt% PEO solution, the observed values of $\overline{\eta}_{e,app}$ are in quantitative agreement with previous measurements using a capillary breakup rheometer [50], despite the instrument not operating at constant extension rate. As no other experimental methods can reliably obtain extensional viscosities at these relatively high extension rates, we can only compare qualitatively the measurements on entangled PEO solutions in highly viscous solvents at lower extension rates [39], where observed strain hardening also results in large increases in extensional viscosity. These results suggest that the in situ PTV measurements allow for quantitatively accurate measurements of the extensional rheology of polymer solutions at rates far exceeding those obtainable by more conventional methods. The model and results shown here demonstrate that the spinning solution's extensional rheology determines the properties of the jet in this stable regime, as shown previously in calculations by Feng [27].

Note that as the extension rates are driven by the applied EMS (stress driven), the range of rates accessible for any given solution is limited by the range of process parameters accessible. However, the addition of electrolyte significantly increases the applied stress, which leads to higher extension rates. Here, the 2 wt% PEO with 1 mM NaCl exhibits extensional thickening for extension rates above 600 s^{-1} (Fig. 13). Again, previous studies of similar solutions also show extensional thickening for concentrations below c_e [39]. Recall that a transition from beaded fibers to continuous fibers is obtained upon addition of salt and increasing EMS, coinciding with extensional thickening. This suggests that strain hardening and extensional thickening

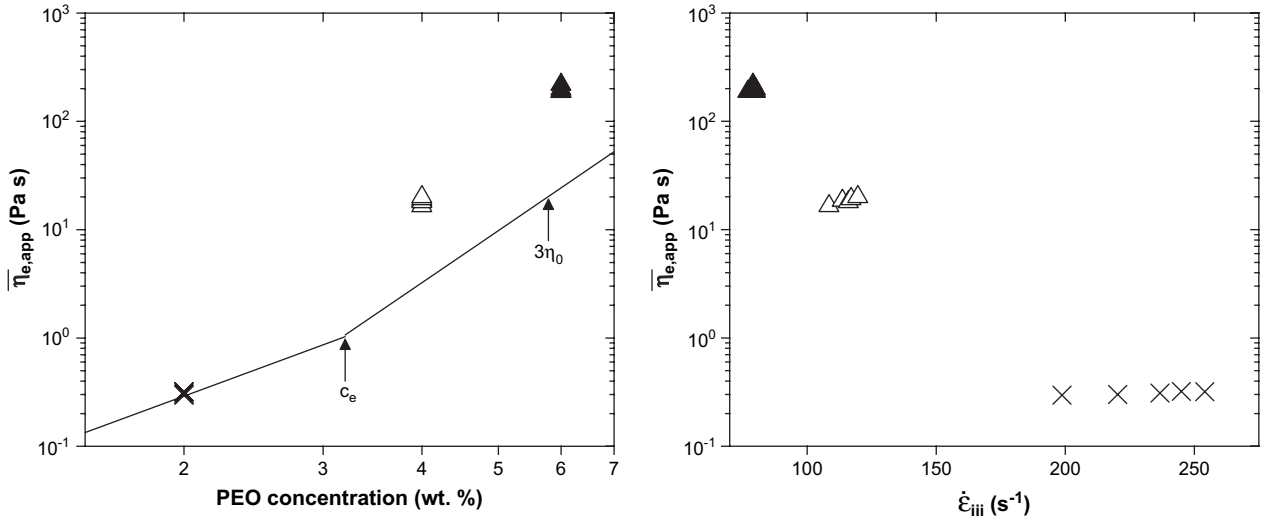

Fig. 12. Apparent extensional viscosity calculated using Eq. (9) versus PEO concentration (left) and jet stretching extension rate (right). Symbols on the right plot correspond to concentrations on the left plot, and the line gives the expected Newtonian extensional viscosity.

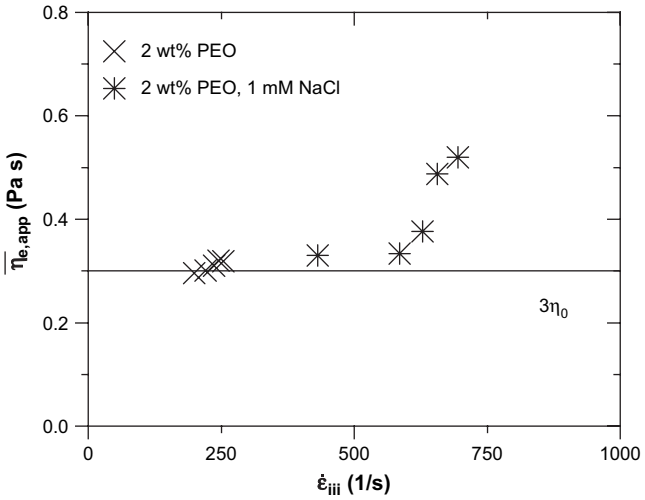

Fig. 13. Apparent extensional viscosity calculated using Eq. (9) for 2 wt% PEO with the NaCl concentrations indicated.

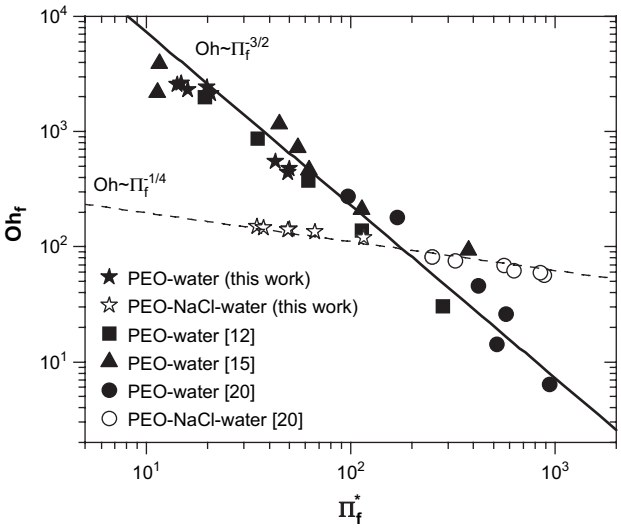

Fig. 14. Ohnesorge number versus jet stretching number for electrospun PEO fibers from solutions of PEO in water (solid symbols) and the electrolyte solutions indicated (open symbols) both from the literature and this work. The lines are empirical scaling relations.

may be prerequisites for the formation of continuous fibers, which may occur even below c_e, contrary to previous hypotheses [46].

5.2. Relation to final fiber morphology

Predictions of final electrospun fiber diameters typically involve a correlation with a single material parameter, such as the zero-shear viscosity of the electrospun polymeric fluid [6–8]. Although such approaches provide empirical scaling for a particular fluid, they are not universal across different polymers and solvents, as they do not take into account the apparent role of extensional rheology on the electrospinning process. Recently, a semi-empirical dimensional analysis of the electrospinning process was used to obtain a single correlation for the electrospun fiber diameter across a variety of different polymer–solvent systems under a wide range of operating conditions [45]. The two important quantities used in the dimensional analysis were an electroviscous number, $\Pi_1 = 2\bar{\varepsilon}^2 E_0^2/K\eta_0$, characterizing the strength of the electromechanical stress relative to the shear stress, and the Ohnesorge number, $Oh_f = \eta_0/(\rho\gamma R_f)^{1/2}$, which contains the electrospun fiber diameter, R_f.

One deficiency in the previous analysis [45] was the choice of an electrokinetic time scale for use in Π_1, resulting in values of Π_1 of $O(10^{-8})$ and lower for typical systems. This low value suggests that the wrong physical process was selected to normalize the process time scale. The simplified EHD model in this work identifies the dimensionless group $\Pi_\infty = (\varepsilon - \bar{\varepsilon})E_0^2 R_0^3/\eta_{e,\infty}^+ Q$ as a characteristic stress ratio controlling the straight portion of the jet. This dimensionless group explicitly contains the extensional rheology of the spinning fluid, which is known to control uniform fiber formation. Also, the group uses the convective time scale R_0^3/Q rather than the electrokinetic time scale, while at the same time incorporating the process flow rate, which was absent in the previous analysis despite its known importance in determining the stability of the jet [19]. Thus, the analysis here identifies the alternative dimensionless parameter Π_∞ for correlating electrospun fiber morphology with process parameters.

Based on the analysis presented in this work, we construct a dimensionless plot (Fig. 14) of the Ohnesorge number Oh_f versus Π_f^* for several sets of electrospinning data for aqueous PEO taken from the literature [12,20,44]. Here, the subscript f denotes calculation of the dimensionless groups with respect to the final, measured fiber radius, R_f, as no measurements of R_0 were made in the previous work. Further more the superscript * denotes the use of the reported zero-shear viscosity and the limiting relationship $\eta_{e,\infty}^+ = 3\eta_0$ to estimate the extensional viscosity, as no measurements of the extensional viscosity were made for the literature data. From the results presented here and reported measurements [35], this assumption describes the extensional viscosity at the onset of the process, but underestimates the extensional viscosity at the end of the process. We acknowledge that these assumptions may affect the resulting correlation; nevertheless, excellent correlation of the data for the aqueous PEO solutions probed here and from the literature is observed, validating the approach.

The results follow a power law for several decades in both parameters where $Oh_f \propto \Pi_f^{-3/4}$. This yields the following empirical relationship for the final fiber diameter:

$$R_{fiber} \propto \sqrt{w_p}\left(\frac{\rho\gamma}{\eta_0^2}\right)^{2/7}\left(\frac{\pi\eta_{e,\infty}^+ Q}{(\varepsilon - \bar{\varepsilon})E_0^2}\right)^{3/7}, \tag{10}$$

where $R_f = R_{fiber}(w_p)^{-1/2}$ is the "wet" fiber radius [26] and w_p is the mass fraction of polymer in solution. We note that the correlation as presented uses the final fiber radius, which assumes direct proportionality between the jet radius set in straight portion of the jet and the final radius, which is further reduced by jet thinning and instabilities [18]. The actual relationship between the straight jet radius and the final fiber radius may depend upon the spinning solution as the mechanics of the bending instability involve additional material properties such as conductivity. However, given the validity of the correlation, it is plausible that the jet stretching regime sets the characteristic scale for these downstream processes. Furthermore, as Oh_f and Π_f^* contain only measurable fluid properties, correlations such as those shown in Fig. 14 should be applicable across different materials. This would be a significant improvement over the correlation developed by Fridrikh et al. [26], for which model parameters applicable to polycaprolactone fibers were less successful in correlating fiber diameter for other materials.

Testing the universality of this result would require additional measurements of jet kinematics across a broad range of polymers and solvents. However, the specific effects of increasing conductivity on this correlation can be tested using the data from the solutions with added electrolyte. The data correlate over a large range

of properties (Fig. 14), but with a different power law exponent, namely $Oh_f \propto \Pi_f^{*-1/4}$. This is most likely due to the influence of the bending instability on the final fiber radius, which has been shown [19,23] to depend on the solution conductivity. Specifically, the maximum growth rate of bending predicted by Hohman et al. [23] is inversely proportional to the solution conductivity. As the correlation relies on proportionality between R_f and R_0, a change in the bending instability with large changes in solution properties can be expected to alter the relationship.

6. Conclusions

In this work, we present a simplified electrohydrodynamic model for stable electrospinning jets that identifies flow regimes with simple scaling laws for the jet kinematics. The results are a simplification of more comprehensive approaches [19,23,25,27], and provide a physical framework for jet initiation, stretching, and thinning in the straight portion of the jet. Measurements of the jet kinematics demonstrate that the model captures the dominant physical mechanisms governing the process and validate the slender body assumption. The general features of electrospinning jets predicted by the EHD model are observed for solutions both above and below the entanglement concentration, even when the solution conductivity is varied over an order of magnitude. Measurements of the jet kinematic parameters R_0, n, z_{iii}, and $\dot{\varepsilon}_{iii}$ allow the reduction of an entire jet profile to several key parameters that can be compared quickly and efficiently across different materials and process conditions. Although the current work presents results for polymer solutions, the measurements and analysis shown here should be applicable to other electrospinning fluids as long as the slender body assumption is satisfied. Such wide applicability and reduction in model complexity may aid in the future development of control schemes for electrospinning processes.

The analysis and comparison of model to experiments identify the crucial role of the spinning fluid's extensional viscosity, and especially strain hardening, on jet kinematics and final fiber diameter. Importantly, the flow kinematic measurements also provide the first quantitative in situ measurements of the apparent steady state extensional viscosity of the electrospinning fluid. In agreement with expectation, the apparent, limiting extensional viscosity is three times the shear viscosity for solution concentrations below the entanglement concentration, but exhibits significant increases above this value for concentrations above the entanglement concentration. These results suggest that electrospinning may be used to measure extensional rheology at rates exceeding the range of conventional extensional rheometers for a wide range of fluids over a limited range of applied electromechanical stresses. Such measurements may prove more robust than other techniques that produce high extension rates, such as opposed-orifice devices, which typically suffer from strong entry flows [51] and loss of purely extensional flow at higher rates [34], both of which are absent in electrospinning.

The theoretical and quantitative tools developed in this work also provide a semi-empirical method for predicting electrospun fiber diameter from solution spinning properties and controlled process variables. In particular, a correlation is observed between the Ohnesorge number based on the final fiber diameter and the dimensionless electromechanical stress, Π_f^*, that explicitly incorporates the extensional viscosity. This correlation holds across a broad range of spinning solution concentrations and applied voltages, and may prove more robust than previous approaches [26]. However, because the correlation changes upon addition of a significant amount of electrolyte, this result suggests the importance of considering downstream processes, such as the bending instability, in setting the final fiber morphology. These results are of practical relevance for production of materials by electrospinning and lead to new correlations that warrant further investigation.

Acknowledgements

The authors gratefully acknowledge the help of the Delaware Center for Composite Materials and C. Ni and F. Kriss of the Keck Electron Microscopy Facility. We would also like to thank G.C. Rutledge for helpful discussions. Financial support for this work was provided by the National Science Foundation NIRT program, DMR-0210223. Rheological measurements were performed on an instrument obtained under ARO award W911NF-05-1-0234. Any opinions, findings, and conclusions or recommendations expressed in this material are those of the author(s) and do not necessarily reflect the views of the Army Research Office.

References

[1] Huang ZM, Zhang YZ, Kotaki M, Ramakrishna S. Composites Science and Technology 2003;63(15):2223.
[2] Boland ED, Wnek GE, Simpson DG, Pawlowski KJ, Bowlin GL. Journal of Macromolecular Science: Pure and Applied Chemistry 2001;38(12):1231.
[3] Lim TC, Kotaki M, Yang TKJ, Fujihara K, Ramakrishna S. Materials Technology 2004;19(1):20.
[4] Choi SW, Jo SM, Lee WS, Kim YR. Advanced Materials 2003;15(23):2027.
[5] Kim C, Yang KS, Lee WJ. Electrochemical and Solid State Letters 2004;7(11): A397.
[6] Gupta P, Elkins C, Long TE, Wilkes GL. Polymer 2005;46(13):4799.
[7] McKee MG, Elkins CL, Long TE. Polymer 2004;45(26):8705.
[8] McKee MG, Wilkes GL, Colby RH, Long TE. Macromolecules 2004;37(5): 1760.
[9] Carroll CP, Joo YL. Physics of Fluids 2006;18(5).
[10] Salalha W, Dror Y, Khalfin RL, Cohen Y, Yarin AL, Zussman E. Langmuir 2004; 20(22):9852.
[11] Drew C, Wang XY, Samuelson LA, Kumar J. Journal of Macromolecular Science: Pure and Applied Chemistry 2003;A40(12):1415.
[12] Daga VK, Helgeson ME, Wagner NJ. Journal of Polymer Science Part B: Polymer Physics 2006;44(11):1608.
[13] Caruso RA, Schattka JH, Greiner A. Advanced Materials 2001;13(20):1577.
[14] A. Formhals, 1934–1944.
[15] Deitzel JM, Krauthauser C, Harris D, Pergantis C, Kleinmeyer J. Polymeric nanofibers, vol. 918; 2006. p. 56.
[16] Reneker DH, Yarin AL, Fong H, Koombhongse S. Journal of Applied Physics 2000;87(9):4531.
[17] Yarin AL, Kataphinan W, Reneker DH. Journal of Applied Physics 2005; 98(6).
[18] Shin YM, Hohman MM, Brenner MP, Rutledge GC. Applied Physics Letters 2001;78(8):1149.
[19] Hohman MM, Shin M, Rutledge G, Brenner MP. Physics of Fluids 2001;13(8): 2221.
[20] Fong H, Chun I, Reneker DH. Polymer 1999;40(16):4585.
[21] Saville DA. Annual Review of Fluid Mechanics 1997;29:27.
[22] Yarin AL, Koombhongse S, Reneker DH. Journal of Applied Physics 2001;89(5): 3018.
[23] Hohman MM, Shin M, Rutledge G, Brenner MP. Physics of Fluids 2001;13(8): 2201.
[24] Spivak AF, Dzenis YA. Applied Physics Letters 1998;73(21):3067.
[25] Feng JJ. Physics of Fluids 2002;14(11):3912.
[26] Fridrikh SV, Yu JH, Brenner MP, Rutledge GC. Physical Review Letters 2003; 90(14).
[27] Feng JJ. Journal of Non-Newtonian Fluid Mechanics 2003;116(1):55.
[28] Hayati I. Colloids and Surfaces 1992;65(1):77.
[29] Larrondo L, Manley RSJ. Journal of Polymer Science, Part B: Polymer Physics 1981;19(6):921.
[30] Bellan LM, Craighead HG, Hinestroza JP. Journal of Applied Physics 2007; 102(9).
[31] Lopez-Herrera JM, Ganan-Calvo AM. Journal of Fluid Mechanics 2004;501:303.
[32] Taylor G. Proceedings of the Royal Society of London 1969;313:453.
[33] Laun HM, Schuch H. Journal of Rheology 1989;33(1):119.
[34] Macosko CW. Rheology: principles, measurements, and applications. New York: Wiley-VCH; 1994.
[35] Anna SL, McKinley GH, Nguyen DA, Sridhar T, Muller SJ, Huang J, et al. Journal of Rheology 2001;45(1):83.
[36] Yarin AL, Koombhongse S, Reneker DH. Journal of Applied Physics 2001;90(9): 4836.
[37] Kirichenko VN, Petrianovsokolov IV, Suprun NN, Shutov AA. Doklady Akademii Nauk SSSR 1986;289(4):817.
[38] Reznik SN, Yarin AL, Theron A, Zussman E. Journal of Fluid Mechanics 2004; 516:349.
[39] Yu JH, Fridrikh SV, Rutledge GC. Polymer 2006;47(13):4789.

[40] He JH, Wan YQ, Yu MY. International Journal of Nonlinear Sciences and Numerical Simulation 2004;5(3):243.
[41] Rutledge GC, Fridrikh SV. Advanced Drug Delivery Reviews 2007;59(14):1384.
[42] Daga VK, Wagner NJ. Rheologica Acta 2006;45(6):813.
[43] Helgeson ME, Grammatikos KN, Deitzel JM, Wagner NJ. In: Proceedings of SAMPE, Baltimore; 2007.
[44] Deitzel JM, Kleinmeyer J, Harris D, Tan NCB. Polymer 2001;42(1):261.
[45] Helgeson ME, Wagner NJ. AIChE Journal 2006;53(1):51.
[46] Shenoy SL, Bates WD, Frisch HL, Wnek GE. Polymer 2005;46(10):3372.
[47] Arayanarakul K, Choktaweesap N, Aht-ong D. Macromolecular Materials and Engineering 2006;291(6):581.
[48] Denn MM. In: Pearson JRA, Richardson SM, editors. Computational analysis of polymer processing. New York: Applied Science Publisher; 1983 [chapter 6].
[49] McKinley GH, Sridhar T. Annual Review of Fluid Mechanics 2002;34:375.
[50] Reneker DH, Yarin AL, Zussman E, Xu H. Advances in Applied Mechanics, vol. 41; 2007. p. 43.
[51] Mackay ME, Astarita G. Journal of Non-Newtonian Fluid Mechanics 1997; 70(3):219.